Lab on a Chip

PAPER

View Article Online
View Journal | View Issue

Cite this: *Lab Chip*, 2025, **25**, 2376

Microfluidic artery-on-a-chip model with unidirectional gravity-driven flow for high-throughput applications†

H. Ehlers, [ab] T. Olivier,[a] S. J. Trietsch,[a] P. Vulto,[a] T. P. Burton[a] and L. J. van den Broek *[a]

Cardiovascular disease (CVD) is the leading cause of death worldwide, with a noticeable decline in the approval of new therapeutic interventions. Currently, there is no gold standard for developing new therapies for CVDs, and preclinical models do not translate to clinical efficacy. Therefore, there is an urgent need for *in vitro* models that more accurately mimic human disease processes. Here we describe a model of the artery consisting of monocultures of human coronary artery endothelial cells (HCAECs) or cocultures of HCAECs with human coronary artery smooth muscle cells (HCASMCs). The model was established in the OrganoPlate® 2-lane-48 UF, a novel microfluidic device, comprised of a microtiter plate footprint with 48 chips. Fluid is circulated in a unidirectional manner by interval rocking. The creation of an air–liquid interface at the inlets at a given inclination is used to select flow paths and establish flow in one direction only, whilst capillary forces ensure the channel remains filled with fluid. We investigated the impact of unidirectional or bidirectional flow conditions. Under unidirectional flow, endothelial cells aligned with the flow direction, decreased fibronectin deposition, and smooth muscle cells presented a non-contractile phenotype, emulating the characteristics of healthy arteries. Contrarily, bidirectional flow mimicked features of early endothelial dysfunction, such as contractile morphology of vessels and increased fibronectin secretion, ICAM-1 staining, and lipid deposits. Vascular inflammation could be induced by the addition of TNFα and IL-1β in both flow conditions. Overall, the OrganoPlate® 2-lane-48 UF is a powerful platform providing both throughput and improved flow control, for creating more physiological models. Its ability to replicate key features of a healthy and diseased artery, its potential use in drug screening, and its compatibility with lab automation make it an invaluable tool for researchers aiming for more accurate and efficient therapeutic development in CVD.

Received 30th December 2024,
Accepted 3rd April 2025

DOI: 10.1039/d4lc01109k

rsc.li/loc

Introduction

Cardiovascular disease (CVD) is a leading cause of death globally, accounting for 32% of deaths annually, while drug approvals for CVD therapies have been decreasing in recent years.[1,2] Often, CVDs are developed over a lifetime with contributing factors influencing obesity, diabetes, smoking, and hypertension.[3] Currently, most CVDs are treated with drugs, such as statins, despite poor efficiency.[4] Limited translation of preclinical models, in terms of safety and efficacy, has been reported as a factor in the decline of new therapies. In the vascular system, chronic inflammation or loss of homeostasis leads to the development of endothelial dysfunction and later CVDs, in particular, atherosclerosis.[5–7] The innermost layer of all blood vessels is composed of endothelial cells, which are sensitive to environmental cues like shear stress.[7,8] Smooth muscle cells (SMCs) surround the endothelial cells and are responsible for regulating vascular tone in response to cues from the endothelial cells. Fluid flow plays a crucial role in maintaining vascular homeostasis.[9] Laminar flow promotes a noninflammatory state with elongated endothelial cell alignment in the direction of flow, a vasodilated state, low SMC activation, and low fibronectin secretion.[10,11] In contrast, disturbed flow leads to an increased vasoconstriction, polygonal endothelial morphology, increased expression of inflammatory adhesion molecules, increased lipid uptake, and SMC activation.[10,12,13] In endothelial dysfunction, the smooth muscle cells become activated by increased lipid uptake and migrate to areas of inflammation.[14] This positive feedback loop leads to the recruitment of immune cells and lipid droplet accumulation, culminating in atherosclerosis, which involves

[a] *Mimetas B.V., Oegstgeest, The Netherlands. E-mail: l.vandenbroek@mimetas.com*
[b] *Leiden Academic Centre for Drug Research, Leiden University, Leiden, The Netherlands*

† Electronic supplementary information (ESI) available. See DOI: https://doi.org/10.1039/d4lc01109k

plaque formation and reduces blood flow and oxygen supply to the vital body organs.[5] Current treatment options for atherosclerosis treat the symptoms (*e.g.*, high cholesterol or high blood pressure),[15] but do not address the underlying mechanism of action. Therefore, better models for disease progression and therapies need to be developed.

There is no gold standard model for mimicking endothelial dysfunction because animal nor *in vitro* models fully recapitulate the disease pathology. Several mouse models have been developed, such as ApoE−/− or eNOS knockout, each of which has their drawbacks.[16] In general, animals have poor translation to humans due to different genetics and mechanisms of disease progression.[17] Therefore, there is a pressing need to develop new, standardizable methods for CVD modeling in drug screening.[18–20] Recently, microfluidic models have tried to bridge the gap between 2D cell culture and *in vivo* models.[21] These so-called organs-on-a-chip offer a route to create complex models of human disease[22,23] To reduce the use of animal models for drug testing, the FDA Modernization Acts 2.0 and 3.0 help to stimulate innovation and lower the barrier to the adoption of such advanced *in vitro* models.[24,25] For example, Zhang *et al.* utilized tissue-engineered blood vessels with endothelial cells and fibroblasts under the physiological flow, enzyme-modified low-density lipoprotein (eLDL), and TNFα to model early-stage atherosclerosis.[26] This model mimicked the immune component of atherosclerosis with the addition of monocytes, and they showed a decrease in inflammation with the addition of a drug. However, this model was low throughput and was not commercially available. Hattori *et al.* investigated impact of three different shear stresses and demonstrate that HUVEC cells aligned with the fluid flow and had an increase in atheroprotective gene expression, like eNOS and THBD, in response to the increase in shear stress.[27] Most microfluidic models that modulate shear stress involve the use of a pump.[27–31] However, the use of a pump makes operation more complicated, limits the throughput, and requires the use of external, often bulky setups. Gravity-driven microfluidic devices have been developed to tackle these downsides. These devices offer benefits over pump-based systems due to their lower complexity, no additional tubing or complex setups, lower initial costs, quicker set-up time, lower footprints, lower reagent volumes, and open well architecture.[32–36] Van Duinen *et al.* showed the culture of 96 blood vessels of which barrier function could be modulated by inflammatory and angiogenic triggers.[37] These and other gravity driven setups typically rely on bidirectional flow, or reversing the fluid flow direction in dependance of the inclination angle. Unidirectional flow setups have also been reported.[35,36,38,39] These microfluidic models obtain unidirectional flow by allowing the fluid to circulate using a circular channel or using angle of inclination to allow the fluid to flow through a separate channel to return to the starting location. This results in a flow pattern comprising of a flow phase and a stall or reset phase in which the fluid is returned to the initial reservoir. Yet these setups are typically based on a single chip setup and have therefore limited value for routine experimentation.

Here, we describe an innovative model of the human *in vitro* artery. The model makes use of a novel microfluidic device, the OrganoPlate® 2-lane-48 UF. The device has 48 microfluidic chips consisting of an extracellular matrix channel, a perfusion channel, and a bypass channel. Flow is induced by gravity through reciprocal rocking, and unidirectional flow paths are selected by capillary force at the air–liquid interfaces, thus preventing backflow. This platform builds on the previous published unidirectional microfluidic models in a higher throughput platform. Monocultures of primary human coronary artery endothelial cells (HCAECs) or cocultures of HCAECs and human coronary artery smooth muscle cells (HCASMCs) vessels were established and placed under unidirectional or bidirectional flow. By utilizing the platforms multiplexing capabilities, cell alignment, marker expression, cytokine release and extracellular matrix secretion were investigated to compare the effects of flow on monoculture and coculture vessels. Additionally, the vessels were exposed to cytokine treatments to study the effects of flow on the vessels ability to respond to inflammation. Overall, we could effectively demonstrate features of healthy and disease coronary arteries. We believe these assays could aid the discovery of novel treatments for cardiovascular diseases.

Methods

Cell culture

Human coronary artery endothelial cells (HCAECs, Promocell, C-12221) were thawed in a T75 flask and cultured at 37 °C, 5% CO_2 in MV2 medium (Promocell, C-22022). HCAECs were cultured until passage 5 and frozen in MV2 + 5% FBS + 10% DMSO for later use. Human coronary artery smooth muscle cells (HCASMC, Promocell, C-12511) were thawed in a T75 flask and cultured at 37 °C, 5% CO_2 in smooth muscle cell growth medium 2 (Promocell, C-22060) until passage 4. HCASMCs were frozen in MV2 + 5% FBS + 10% DMSO for later use. For each experiment, HCAECs and HCASMCs were thawed into the flask and cultured in their respective medium at 37 °C, 5% CO_2, until they reached confluency.

OrganoPlate 2-lane-48 UF and 2-lane-48 UF bidirectional control

Mimetas OrganoPlate® 2-lane-48 UF (Fig. 1A) comprises a bypass channel, a cell culture channel that is separated from a gel channel by means of a capillary pressure barrier, as previously described.[40] The bypass channel dimensions have a thicker width, at 1.2 mm, to allow for a lower channel resistance and reduce the reset period of the system. To create one long well, the device uses a custom 384-well titer plate where 3 wells are merged in columns 1–3, 6–8, 9–11, 14–16, 17–19, and 22–24. Columns 4, 12, and 20 are for hydrogel seeding, and columns 5, 13, and 21 are the

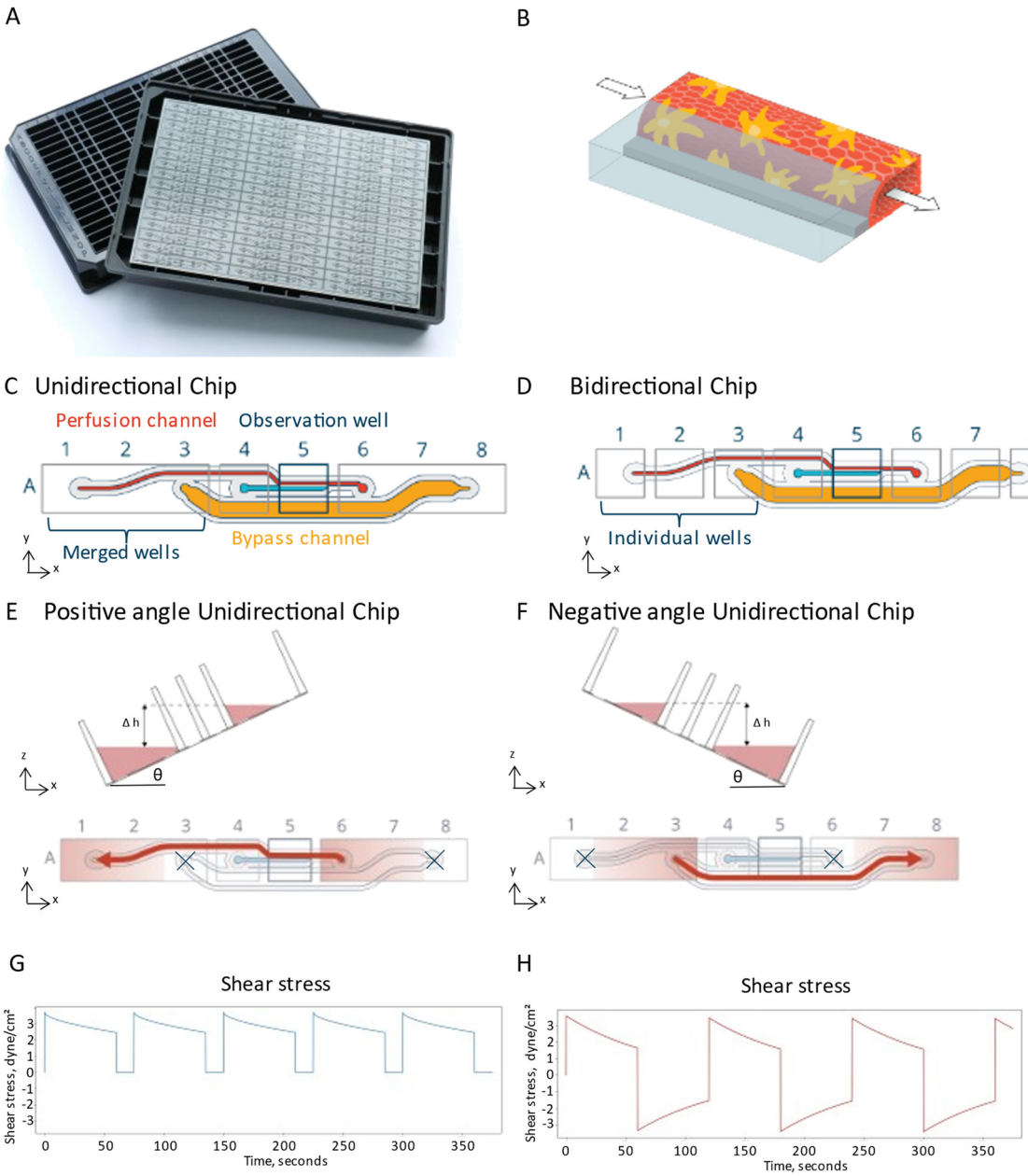

Fig. 1 Unidirectional flow microfluidic device with the comparable bidirectional microfluidic device. (A) OrganoPlate 2-lane-48 UF consists of 48 individual microfluidic chips. (B) Schematic of perfusable blood vessel consisting of endothelial and smooth muscle cells under unidirectional flow. (C) Schematic of OrganoPlate 2-lane-48 UF chip design. Three wells of 384 well titer plate were combined to create one large well (columns 1–3 and 6–8). Cells were seeded in the perfusion channel (red). Bypass channel (yellow) is used to return the medium to starting well. The large well allows the medium from the perfusion channel to pass through the bypass channel. (D) Schematic of bidirectional chip design. Standard 384 well plate is used with no combined wells. Therefore, there is no medium exchange between the perfusion and bypass channels. (E) Schematic of positive angle perfusion of the OrganoPlate 2-lane-48 UF chip allows fluid flow from the right side of the chip to the left through the perfusion channel containing cells. (F) Schematic of the negative angle perfusion on the OrganoPlate 2-lane-48 UF chip allowing for fluid flow from the left side of the chip to the right side of the chip through the bypass channel. (G) Graph of the simulated shear stress in the unidirectional microfluidic chip. (H) Graph of the simulated shear stress in the bidirectional microfluidic chip.

observation wells. This allows each chip to consist of 2 long wells, a gel seeding well, and an observation well (Fig. 1C). The plate consists of a total of 48 chips. The long well and a lower media volume allow for creating an air–liquid interface above the outermost holes in the chip at positions 3 and 8 (Fig. 1E) when the plate is angled above a critical angle. The formation of an air–liquid interface above an inlet hole prevents fluid flow, the size constraints of the device result in a Laplace value, and surface tension prevents the microfluidic channel from emptying. When the angle of inclination is positive, fluid is routed through the cell culture channel (Fig. 1E). When the angle of inclination is negative,

fluid is routed through a bypass channel, resetting the system (Fig. 1F). For the bidirectional plate, a standard 384-well titer plate was used as the top part (Fig. 1D). For the bottom part, the 2-lane UF bidirectional plate used the same microfluidics as the OrganoPlate® 2-lane UF. Without the long channels, the medium in the perfusion channel cannot pass through the bypass channel and flows back through the perfusion channel. This creates bidirectional flow through the perfusion channel.

OrganoPlate seeding and unidirectional flow

For seeding of the ECM, 1.1 μL of a gel composed of 4 mg mL^{-1} collagen-I (Cultrex 3D collagen-I rat tail, 5 mg mL^{-1}, 3447-020-01, AMSbio), 100 mM HEPES (15630-122, Thermo Fisher, Waltham, MA, USA) and 3.7 mg mL^{-1} $NaHCO_3$ (Sigma, S5761) was dispensed in the gel inlet. The OrganoPlate was incubated for 15 min at 37 °C. After gel polymerization, 50 μl of HBSS was added to the gel inlet and observation well. Plates were stored in an incubator at 37 °C, 5% CO_2 overnight. HCAECs and HCASMCs were harvested using trypsin + 0.25 EDTA (Lonza, CC-5012) and neutralized with trypsin neutralizing solution (Lonza, 5002). All conditions were spun down at 220*g* for 5 minutes. Cultures were resuspended to a density of 10 000 HCAECs per μl and 2500 HCASMCs per μl. For coculture conditions, HCAECs and HCASMCs were combined at a ratio of 4 : 1, respectively. The 4 : 1 ratio of ECs to SMCs was determined to lead to the most stable vessel over time in previous studies and model optimization (data not shown here). To seed the cells, 50 μl of MV2 medium was added to the perfusion outlet and 1 μl of the cell suspension to the perfusion inlet. Plates were incubated at a 75° angle for 2 hours to allow cell attachment before adding 50 μl of MV2 medium to the perfusion outlet and 100 μl to the perfusion inlet for the unidirectional conditions. For the bidirectional conditions, 50 μl of MV2 medium was added to the perfusion inlet, bypass inlet, and bypass outlet (Table S1†). Plates were placed at OrganoFlow® 2.0 with the setting of 7° 8 minute, herein called the growth rocker setting, for 3 days. This growth setting ensures that both conditions form a confluent tube before being placed in their respective high-shear rate condition. These settings have previously been used in the OrganoPlate to generate endothelial tubes with leak-tight barriers.[41] Medium change was performed where 40 μl of MV2 medium was added to the perfusion inlet and outlet. Unidirectional conditions were placed on the asymmetric rocker with a 25° 1 minute interval for a positive angle and a 25° 15 second interval for a negative angle. Bidirectional conditions were placed on a symmetric 25° 1 minute interval rocker (Table S1†). At day 4 of the culture, specific chips were exposed to cytokines for 24 hours. For the cytokine exposure, TNFα (R&D Systems, 210-TA-020) and IL-1β (ImmunoTools 11340013) were diluted in MV2 medium to 1 ng ml^{-1}. On days 3 to 5 of culture, all chips of the OrganoPlates were imaged for 4× magnification phase contrast images at the ImageXpress Micro XLS microscope (molecular devices). On day 5 of the culture, the OrganoPlates were fixed in 3.7% formaldehyde in HBSS with calcium and magnesium (Sigma, 252549) and stored at 4 °C.

Immunofluorescent staining and imaging

After fixation, cultures in the OrganoPlate were stained for immunofluorescent markers, as described previously.[42] In short, cells were permeabilized using a Triton X-100 solution for 15 min and blocked using a buffer containing FBS, bovine serum albumin, and Tween-20 for 45 min. Primary antibodies were incubated overnight, after which secondary antibodies were incubated for 2 hours. The following primary antibodies were used to stain fixed cultures: anti-VE-cadherin 1 : 500 (Abcam, ab33168), anti-ICAM-1 1 : 50 (R&D systems, BBA3), anti-human CD31 1 : 160 (Dako, M0823), fibronectin 1 : 100 (Sigma, F3648) and αSMA 1 : 500 (Sigma, A2547). The following secondary antibodies were used: goat anti-rabbit IgG (H + L) Alexa Fluor 555 1 : 250 (Thermo Fischer Scientific, A21428), goat anti-mouse IgG (H + L) Alexa Fluor 647 1 : 250 (Biotium, 20040). Additionally, BODIPY 1 : 760 (Thermo, D3922) and actin green (2 drops per ml) (Thermo, R37110) were added to secondary antibodies. Nuclei were stained using Hoechst (ThermoFisher, H3570). After staining, the OrganoPlate was transferred to a confocal high-content imaging microscope for automated imaging (Micro XLS-C, molecular devices). Images were acquired at 10× magnification at 5 μm increments along the height of the microfluidic channel. Analysis was based on sum projection (ICAM expression, fibronectin, BODIPY) of the entire vessel or Max projection (CD31, actin, VE-cadherin) images of the bottom 10 z-slices.

Image analysis

Images were cropped to the same dimensions using a macro in ImageJ that created the same box for all images. Nuclei were counted using an automated ImageJ nuclei counting tool developed in-house. ICAM-1, fibronectin, and BODIPY immunofluorescent staining quantification was performed as de Haan *et al.* reported in 2021.[43] Directionality was determined using a max projection of only the bottom 10 slices of CD31 to ensure that only a single layer of endothelial cells was analyzed. The directionality tool in the software Fiji was used to quantify alignment.[44] OrientationJ analysis was used to create alignment images of CD31.[45]

For VE cadherin analysis, image analysis was performed using MetaXPress (version 6.7) and IN Carta image analysis software (version 2.1). Images acquired on the ImageXPress Micro Confocal were exported to XMCE format using MetaXPress. Afterward, images were imported into IN Carta, where analysis was conducted. Using the SINAP module, the pre-trained nuclei DCNN[46] was utilized to segment the nuclei from the Hoechst stained image, and masks were generated. For the VE-cadherin signal, two distinct DCNN were trained. One was configured to segment the cellular space between the junctions (negative space), and the second was to segment the stained junctional network itself (positive space).

Morphological, intensity, positional, and textural descriptors were extracted from the DAPI and VE-cadherin images. Supporting data was obtained by applying the negative space VE-cadherin masks to the other markers, measuring intensity and textural descriptors. Further quality control and initial analysis were performed using JMP software 17.2 (SAS Institute Inc., Cary, NC). All objects were checked for faulty or erroneous segmentations. Objects smaller than 5 μm and outside the perfusion channel were excluded from the output. Chip positions were labeled based on their treatment conditions and flow configuration.

IL-6 ELISA

IL-6 release was quantified using an IL-6 ELISA kit (R&D systems, DY206-05). The manufacturer protocol was followed. For non-cytokine exposed samples, coculture samples were diluted 1 : 2 in reagent dilutant, and HCAEC monocultures were not diluted. For cytokine conditions, samples were diluted 1 : 200 in reagent diluent. The standard curve was calculated using the "Interpolated Standard Curve" function in GraphPad Prism software. Sample concentration was determined from the standard curve.

Statistics

Means of two or more groups were assessed using Brown–Forsythe and Welch ANOVA (Gaussian, heterogeneity of variance) or Kruskal–Wallis tests (non-Gaussian) for statistically significant differences. In the case of two or more factors, two-way ANOVA tests were formed depending on the number of factors. Multiple comparisons were accounted for using Tukey's or Dunnett's tests. All data sets were tested for normality using QQ plots and residuals for normality. Statistical analyses were performed using GraphPad Prism v10.4 (GraphPad Software). Differences were considered significant when $p < 0.05$. For the number of replicates, each independent experiment is represented by an "N", and the individual chip is represented by an "n". Total number of replicates is $N \times n$.

Results

OrganoPlate 2-lane-48 UF

Fig. 1 shows the novel OrganoPlate 2-lane-48 UF. It is comprised of a microtiter plate footprint and comprises 48 chips. Each chip comprises two flow paths: a first path comprising the cell culture and a second 'bypass channel' to reset the flow (Fig. 1E and F). The inlets holes of the two flow paths are connected by joining together three wells from the microtiter plate (Fig. 1A and C). The cell culture channel comprises a phaseguide[47] that serves to pattern the hydrogel in one part of the channel and direct the growth of cells against the gel in an adjacent part of the channel, to form a vessel-like structure (Fig. 1B).[40,47] The OrganoPlate 2-lane-48 UF uses passive leveling of fluid to drive flow through the microfluidic channels. The OrganoPlate 2-lane-48 UF is placed on an interval rocker that tilts back and forth. The device uses an asymmetric rocking profile where flow is driven through the cell culture channel by tilting to a 25° angle for 1 minute in the positive direction and subsequently rocked to 25° for 15 seconds in the negative direction to redirect flow through the bypass channel to reset the system. While the rocker moves to the negative angle, there is approximately 7 seconds of backflow before the fluid flow stalls for the remainder of the 15 second reset period. The flow path is selected by the capillary force at the air–liquid interface at the inlet of the fluid channel in which flow is blocked at respective inclination (see Fig. 1E and F). The plate utilizes high angles of inclination to prevent fluid flow through the highest elevated inlet when the plate is tilted above 10°. This directed flow through the cell culture channel (Fig. 1E) or the bypass channel (Fig. 1F). This rocking scheme is repeated throughout the duration of the culture with a simulated peak shear stress of 3.7 dynes per cm^2 (Fig. 1G, ESI† Methods). The unidirectional flow was confirmed using fluorescent beads (Fig. S1†). A second plate serves as bidirectional control, in which the wells of the inlets and outlets of each chip are not joined together. This disconnects the active channel from the bypass channel, resulting in a bidirectional flow (see Fig. 1D). For bidirectional flow, the device uses a symmetric rocking profile, where flow is driven by tilting to a 25° angle for 1 minute in the positive direction followed by 1 minute in the negative direction. The cell culture channel has a simulated peak shear stress of 3.57 dynes per cm^2 (Fig. 1H, ESI† Methods).

Effects of unidirectional and bidirectional flow on human coronary artery endothelial vessels

In the first three days after seeding the endothelial cells in the OrganoPlate, HCAECs were cultured to confluency and formed a complete tubular structure within the microfluidic channel under bidirectional flow. After 3 days, the vessels were confluent with a cobblestone-like, polygonal endothelial morphology for both OrganoPlates (Fig. 2A and B). The unidirectional plate was placed under unidirectional flow conditions on day 3 by changing the rocker to asymmetric rocking and lower the fluid volume. Within 24 hours, the cell morphology changed, with the cells elongating and aligning with the direction of flow (Fig. 2B). The bidirectional control vessels continued to exhibit the cobblestone-like morphology. This was also apparent on day 5 of culture. In line with phase contrast images, the actin filament expression in the unidirectional condition aligned with the flow, whereas the bidirectional conditions did not have uniform actin alignment (Fig. 2C and D). In addition to the cytoskeletal alignment, alignment of the cell body was confirmed using CD31 staining, where the unidirectional flow had a normally distributed alignment with the flow direction, and the bidirectional conditions had little alignment (Fig. 2E). The CD31 junctions in the unidirectional flow appeared thinner and more uniform than the bidirectional conditions, which had wider and fuzzier appearing junctions. Fibronectin, an adhesion glycoprotein

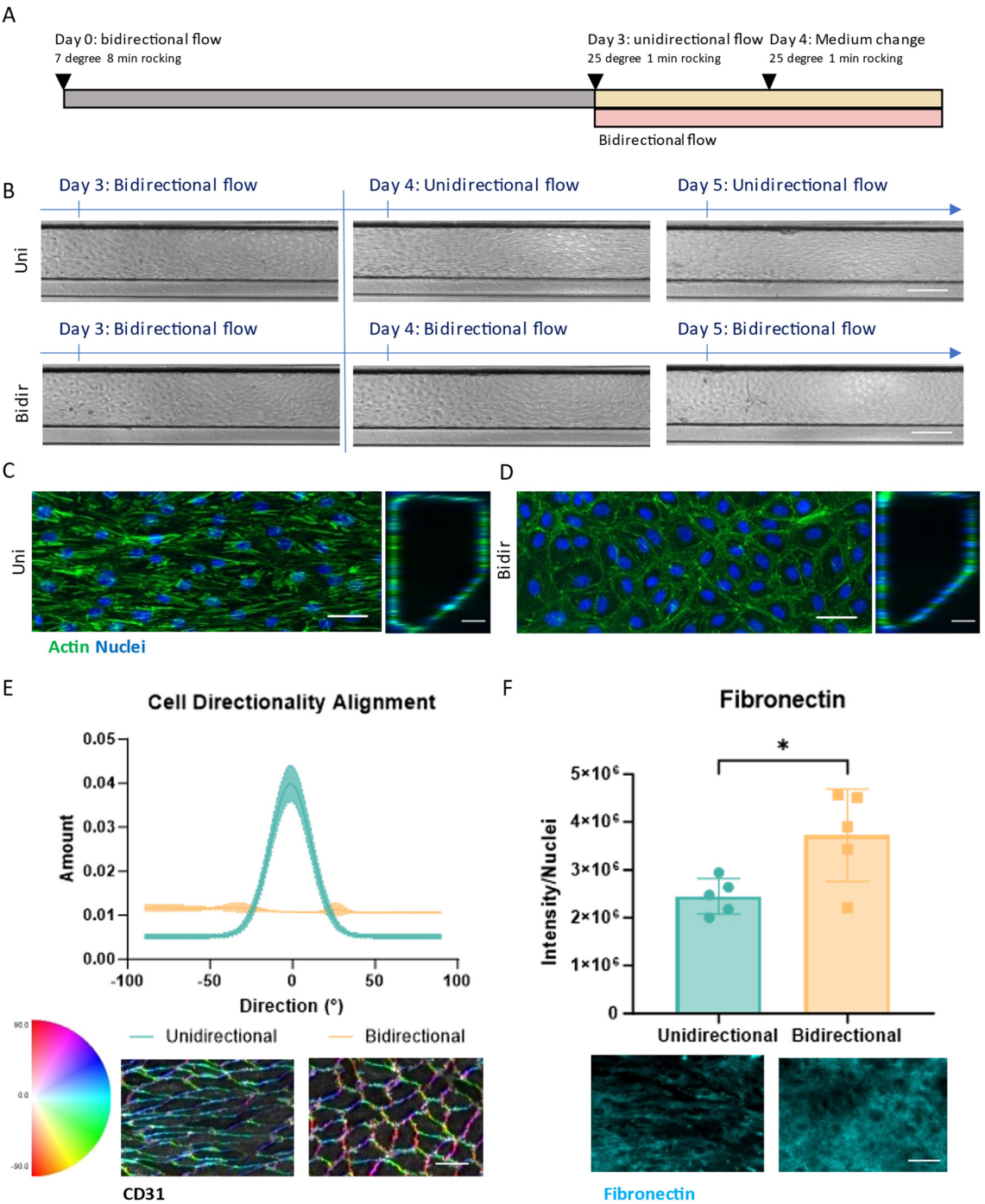

Fig. 2 HCAEC vessel under unidirectional flow *versus* bidirectional flow. (A) Experimental timeline for vessel formation and unidirectional or bidirectional flow. (B) Phase contrast images of HCAECs over time in unidirectional *versus* bidirectional flow (scale bar 200 μm) (N = 3, n = 9). Actin (green) and nuclei (blue) max projection images and 3D reconstructions of (C) unidirectional HCAEC vessel and (D) bidirectional HCAEC vessel (N = 2, n = 2–3) (scale bar 50 μm). (E) Quantification of CD31 alignment in the direction of the flow (N = 2, n = 2–3) and CD31 fluorescent staining of bottom 10 slices of unidirectional HCAEC vessel and bidirectional HCAEC vessel. Color matches directionality in legend on left (scale bar 50 μm). (F) Fibronectin staining and quantification of HCAEC vessel (scale bar 50 μm) (N = 2, n = 2–3). Statistically significant differences were calculated using unpaired T-test (*$p < 0.05$).

involved in maintaining blood vessel morphology, was secreted more in the bidirectional condition than in the unidirectional condition (Fig. 2F). Other markers related to vascular health, IL-6 secretion, lipid accumulation, and ICAM-1 expression were similarly expressed in unidirectional and bidirectional conditions in monoculture vessels (Fig. 3).

The effects of inflammatory cytokines, 1 ng ml^{-1} TNFα + 1 ng ml^{-1} IL-1β were assessed to determine vascular inflammatory

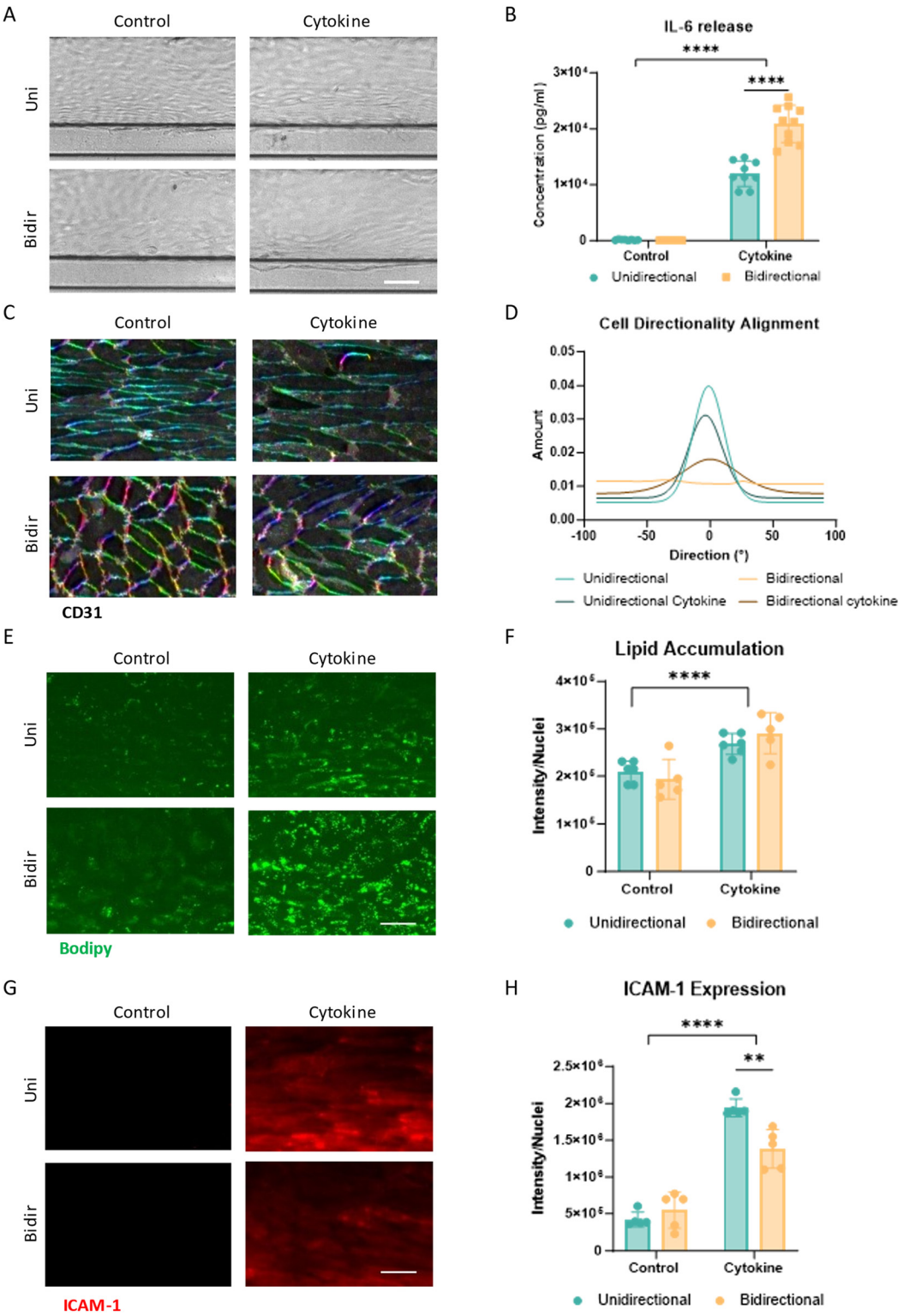

Fig. 3 HCAEC vessels exposed to inflammatory cytokines under unidirectional flow *versus* bidirectional flow. (A) Phase contrast images of HCAEC vessels were exposed for 24 hours to 1 ng ml^{-1} of TNFα + IL-1β under unidirectional and bidirectional flow on day 5 of culture. Scale bar 100 μm. (B) IL-6 release (pg ml^{-1}) of cytokine-exposed HCAEC vessels. Significant difference between control and cytokine conditions (****$p < 0.0001$) as well as between unidirectional and bidirectional cytokine treated conditions (****$p < 0.0001$) (N = 2–3, n = 3–4). (C) CD31 fluorescent staining of the bottom 10 slices of the vessel. Staining color matches directionality in legend in Fig. 2C. Scale bar 50 μm. (D) Quantification of CD31 alignment in the direction of the flow (N = 2, n = 2–3). (E) Lipid droplet fluorescent images by BODIPY of HCAEC vessels. Scale bar 50 μm. (F) Lipid droplet accumulation quantification through BODIPY staining. Significant difference between control and cytokine conditions (****$p < 0.0001$) (N = 2, n = 2–3). (G) ICAM-1 fluorescent image of HCAEC vessels. Scale bar 50 μm. (H) ICAM-1 quantification of HCAEC vessel. Significant difference between control and cytokine conditions (****$p <$ 0.0001) as well as between unidirectional and bidirectional cytokine treated conditions (**$p = 0.002$) (N = 2, n = 2–3). Data was analyzed using two-way ANOVA tests, followed by Tukey's multiple comparison test.

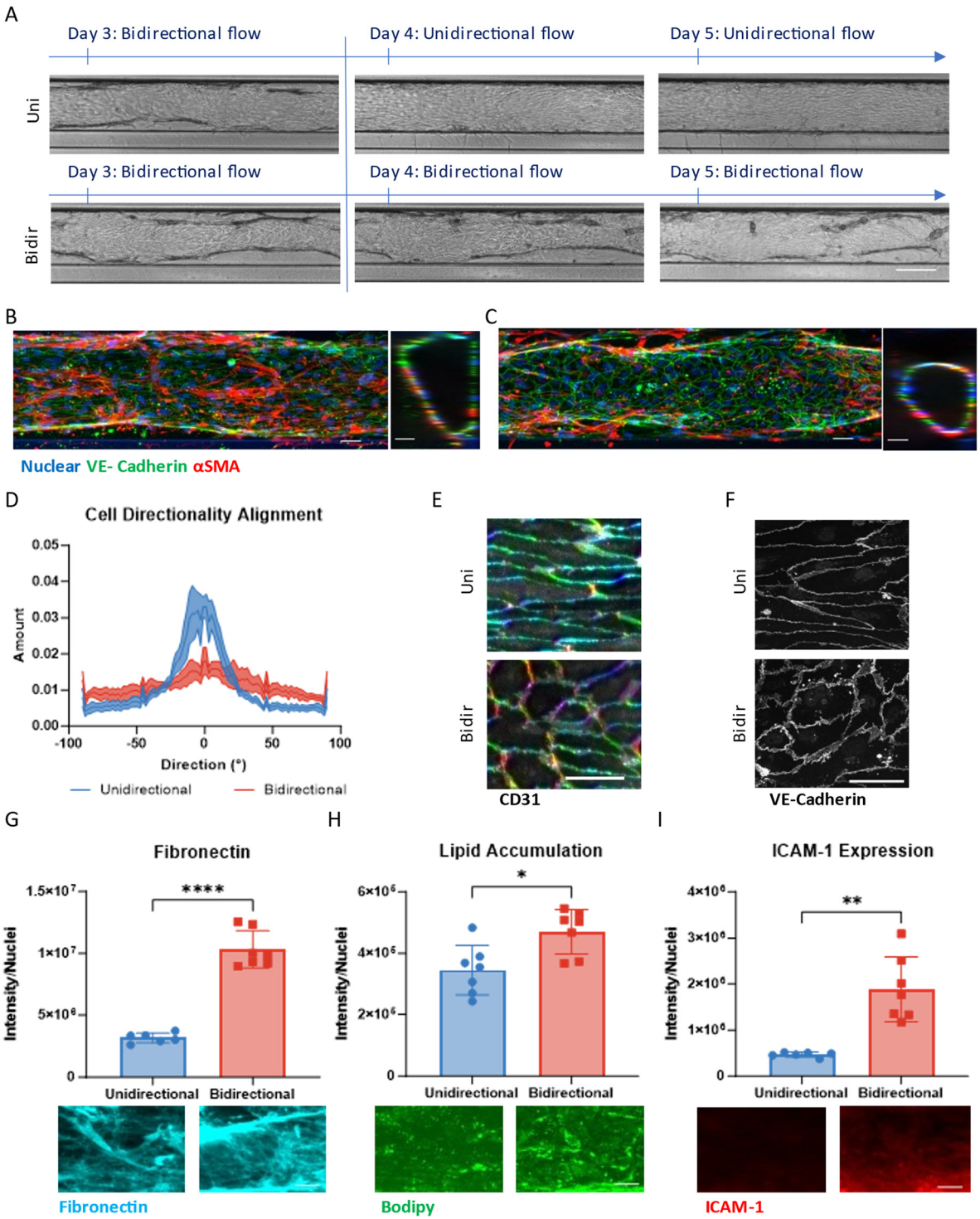

Fig. 4 HCAEC/HCASMC co-culture vessel under unidirectional flow *versus* bidirectional flow. (A) Phase contrast images of HCAECs over time in unidirectional flow *versus* bidirectional flow. Scale bar 200 μm (N = 3, n = 9). Max projection images and 3D reconstructions of (B) HCAEC/HCASMC vessel under unidirectional flow and (C) HCAEC/HCASMC vessel under bidirectional flow. HCAECs were stained with VE-cadherin (green), and HCASMCs were stained with αSMA (red) and cell nuclei with Hoechst (blue) (scale bar 50 μm). (D) Quantification of CD31 alignment in the direction of the flow (N = 2, n = 3). (E) CD31 fluorescent staining of the bottom 10 slices of the vessel. Staining color matches directionality in legend in Fig. 2C. Scale bar 25 μm. (F) VE-cadherin fluorescent staining of bottom 10 slices of the vessel. Scale bar 25 μm. (G) Fibronectin staining and quantification of HCAEC/HCASMC vessel. Scale bar 50 μm. Significant difference between conditions (**$p < 0.005$). Data was analyzed using Welch's T-test (N = 2, n = 2–3). (H) Lipid droplet staining by BODIPY and quantification of HCAEC/HCASMC vessel. Scale bar 50 μM. Significant difference between conditions (*$p < 0.05$). Data was analyzed using an unpaired T-test (N = 2, n = 2–3). (I) ICAM-1 fluorescent staining and quantification of HCAEC/HCASMC vessel. Scale bar 50 μm (N = 2, n = 2–3).

responses under both flow conditions. Upon exposure to inflammatory cytokines, both flow conditions showed changes in cell morphology (Fig. 3A). The cells exposed to unidirectional flow and cytokines widen, and the bidirectional cytokine-exposed cells start to elongate as witnessed by CD31 staining (Fig. 3C). In the unidirectional condition, the vessels exposed to inflammatory cytokines remained aligned with the flow but less aligned than those without cytokines (Fig. 3C and D). Under bidirectional flow, cells exposed to inflammatory cytokines align more with the flow, albeit to a lesser extent than under unidirectional flow. Interestingly, the unidirectional condition showed approximately half the IL-6 release compared to the bidirectional control after 24 hours in culture in conditions exposed to cytokines (Fig. 3B). When exposed to inflammatory cytokines, endothelial cells start to take up lipids, a characteristic of endothelial dysfunction. This increase in lipid accumulation was seen in both cytokine-exposed conditions through an increase in BODIPY lipid dye (Fig. 3E and F). Both conditions showed increased ICAM-1 expression upon inflammatory cytokine exposure, but the unidirectional condition had a higher increase in ICAM-1 expression upon exposure compared to the bidirectional condition (Fig. 3G and H).

Effects of flow on an artery model using human coronary artery endothelial cells and human coronary artery smooth muscle cells

In a next step, human coronary artery smooth muscle cells (HCASMCs) were added to increase the comprehensiveness of the artery model. HCAEC and HCASMCs formed a bilayered vessel, where the HCAECs are surrounded by the HCASMCs (Fig. 4B and C and S2†). Both conditions formed a tubular structure can be seen in the 3D reconstruction (Fig. 4B and C). The cultures were grown for three days under bidirectional flow on the OrganoFlow® 2.0 at the growth rocker setting. After 3 days, the vessels started to show contraction (Fig. 4A). On day 3 plates were placed under unidirectional flow. In these plates, the vessels showed relaxation, covered the microfluidic channel diameter and remained stable for the rest of the culture. In contrast, the plate placed under continued bidirectional flow remained contracted (Fig. 4A).

The alignment of the cells was confirmed using CD31 and VE-cadherin staining (Fig. 4E and F). Similar to monoculture conditions, vessels cultured under unidirectional flow showed alignment with the flow direction, whereas vessels cultured under bidirectional flow showed a more cobblestone-like morphology (Fig. 4D and E). In addition, the VE-cadherin junctions were more linear and less thick or fuzzy when exposed to unidirectional flow compared to the bidirectional control (Fig. 4F). Similar to the HCAEC monoculture, the bidirectional conditions had significantly higher fibronectin secretion when compared to the unidirectional culture (Fig. 4G). Other than in monocultures however, the bidirectional conditions had significantly higher lipid accumulation (Fig. 4H) and ICAM-1 expression (Fig. 4I) compared to vessels grown under unidirectional flow.

Vascular inflammation conditions were induced through exposure to 1 ng ml^{-1} of TNFα + 1 ng ml^{-1} IL-1β for 24 hours. Vessels cultured under unidirectional flow contracted upon cytokine exposure, whereas vessels under bidirectional flow were already contracted before cytokine exposure and did not contract further (Fig. 5A and C). Changes in cell morphology as observed with VE-cadherin staining were comparable to the monoculture vessels (Fig. 5D). For vessels cultured under unidirectional flow, the cells exposed to cytokines were less elongated than non-exposed cells. In contrast, for vessels cultured under bidirectional flow cells exposed to cytokines were elongating and had similar directionality to the unidirectional conditions exposed to cytokines. In addition, the cytokines caused the nuclei in both the unidirectional and bidirectional conditions to elongate (Fig. S3E†). Unidirectional and bidirectional conditions showed increased IL-6 release when exposed to cytokines (Fig. 5B). As seen in monoculture vessels, both unidirectional and bidirectional cytokine exposed conditions significantly increased lipid accumulation and ICAM-1 expression in the vessels compared to the control condition (Fig. 5E and F). Overall, both the unidirectional and bidirectional cocultures showed increased inflammatory characteristics when exposed to cytokines.

Discussion

Here, we report an artery model for healthy and diseased arteries using a coculture model of HCAECs and HCASMCs showing key characteristics of the *in vivo* structure. This microfluidic artery-on-a-chip platform with 48 chips per plate allowed for both unidirectional and bidirectional gravity driven flow. We assessed the impact of flow directionality on vessel morphology, cytokine secretion, and changes in junction markers. In both the unidirectional and bidirectional chips, the peak shear stress was around 3.7 dynes per cm^2 and had flow cycle times of 1 minute. Under unidirectional flow, the endothelial cells aligned with the flow, and the smooth muscle cells presented a noncontractile phenotype that mimicked healthy *in vivo* arteries. Bidirectional flow-induced contractile phenotype in smooth muscle cells and the slightly increased levels of fibronectin, lipid accumulation, and ICAM-1 expression might indicate early signs of endothelial dysfunction. Both flow conditions showed vascular inflammation hallmarks upon exposure to inflammatory cytokines.

In contrast to most other unidirectional vascular model studies, this research was done with primary-derived artery endothelial cells. In line with previous reports on HUVEC vessels, HCAEC vessels under unidirectional flow showed alignment of cytoskeleton and CD31. Thick actin filaments that align with the flow are thought to maintain cell stiffness, which sustains vascular tone.[48,49] We observed that realignment with flow happens within 24 hours, which is in line with previous reports.[50] The lower levels of fibronectin secretion observed under unidirectional flow compared to

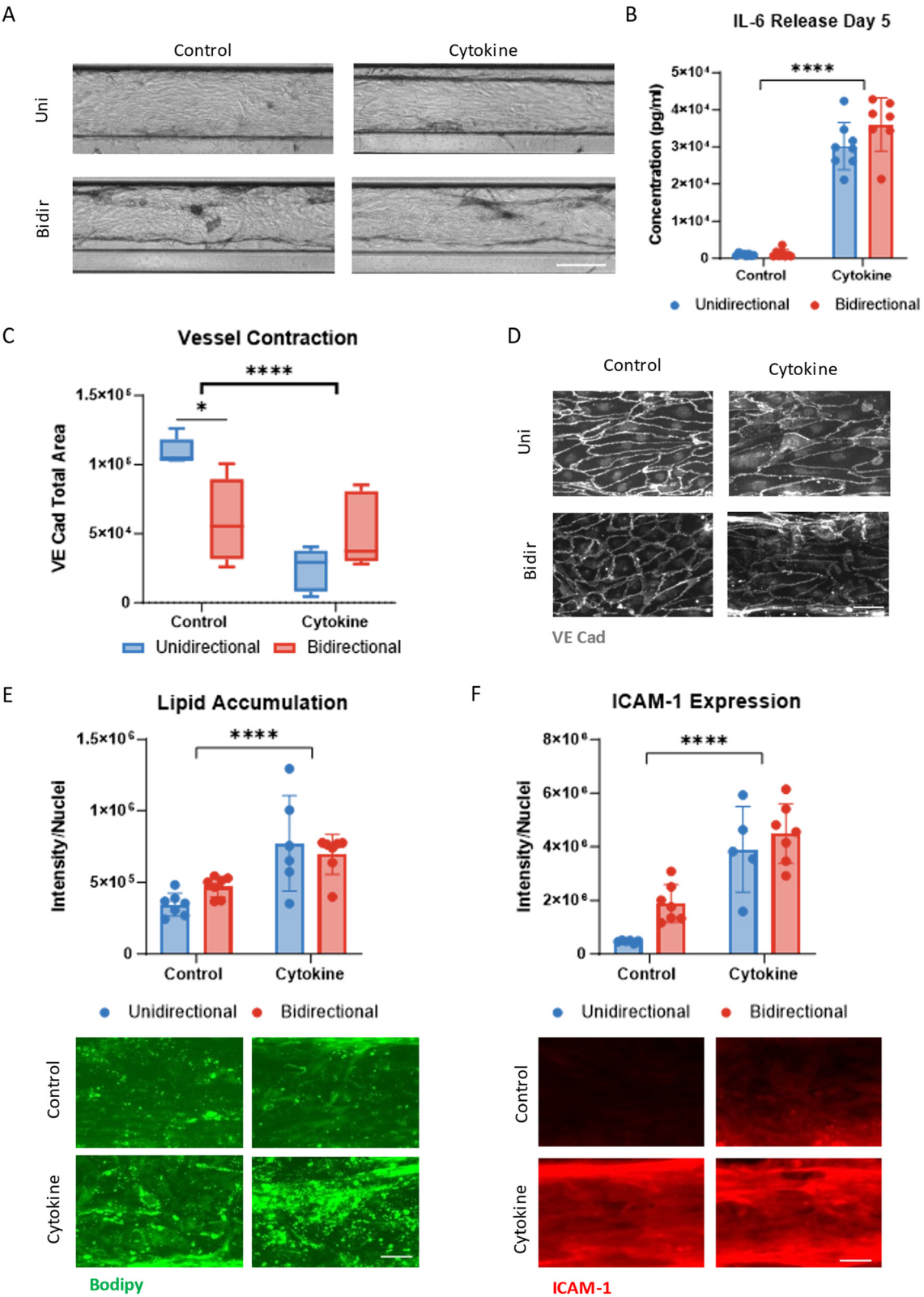

Fig. 5 HCAEC/HCASMC vessel exposed to 1 ng ml^{-1} of TNFα + IL-1β under unidirectional flow *versus* bidirectional flow. (A) Phase contrast images of vessels on day 5 of culture (scale bar 100 μm) (N = 3, n = 9). (B) IL-6 release of cytokine exposed vessel (N = 2, n = 4). (C) Quantification of vessel confluency using VE cadherin total area coverage (N = 2, n = 2–4). (D) VE-cadherin fluorescent staining of the bottom 10 slices of the vessel. Scale bar 50 μm. (E) Lipid droplet accumulation quantification and staining (N = 2, n = 2–3). (F) ICAM-1 quantification and staining of HCAEC/HCASMC vessel (N = 2, n = 2–3). Significant difference between control and cytokine conditions (****$p < 0.0001$). Data was analyzed using two-way ANOVA tests, followed by Tukey's multiple comparisons test.

bidirectional flow in combination with increased alignment might suggest that the vessels cultured under unidirectional flow can be considered more atheroprotective.[51–54] In contrast to Yang *et al.*, no difference was found in the secretion of inflammatory mediator IL-6.[36] This inconsistency could be explained by a difference in shear stress, different cell types used, and different frequencies in the flow cycle. The flow cycle frequency in both studies is much lower compared to *in vivo* flow cycles within arteries, which occur at the same frequency as the heartbeat, approximately 1 Hz at rest.[55]

Previously, HCAECs models in the OrganoPlate have been reported.[56,57] These vessels were grown under bidirectional flow and had cobblestone-like morphology, similar to the monoculture bidirectional control. Results, however, are not directly comparable, because the previously reported models were grown in chips with shorter microfluidic channels and used different rocker settings, with a lower frequency of fluid flow through the microfluidic channel. Similar to the previous HCAEC OrganoPlate models, ICAM-1 expression was increased when exposed to inflammatory cytokines. Also, lipid accumulation and IL-6 secretion were increased for both unidirectional and bidirectional flow conditions when exposed to cytokines.

There is limited literature available that compares fluid flow over a similar time frame in endothelial vessels with comparable readouts. However, existing studies suggest that there would likely be a greater difference between conditions during vascular inflammation than were found here.[11,58] While there was a similar level of IL-6 in healthy monocultures, after cytokine exposure, cells under unidirectional flow produced approximately half the IL-6 compared to cells under bidirectional flow, possibly indicating greater resilience to external stressors. In contrast, ICAM-1 expression was significantly higher under unidirectional flow, a finding that has also been reported in previous studies.[59,60] The flow effect on the HCAEC vessels showed the difference between healthy and slightly atheroprone vessels.

Adding HCASMCs yielded more pronounced differences in flow conditions. The coculture vessels had all contracted by day 3 of culture, which would change the intraluminal shear stress, as it is dependent on the vessel diameter. While not all the vessel contracted uniformly, this change in shear stress might promote an inflamed vessel prior to change of flow conditions. Therefore, the relaxation of the blood vessels after placing them in unidirectional flow indicates that the SMCs reacted to cues from ECs due to the change in flow conditions, causing vasodilation.[61,62] Chiu *et al.* found that shear stress played an important role in inhibiting proinflammatory genes expressed by ECs cultured in close proximity to SMCs.[63] The bidirectional control exhibited a more inflamed state, with higher lipid and ICAM-1 expression, similar to the turbulent region of a blood vessel.[64] Due to the bidirectional flow, the SMCs appeared more activated by causing sustained vessel contraction and a significant increase in lipid accumulation compared to the monoculture conditions.[14] As a result of the vessel contraction, *in vitro* cultures utilizing bidirectional flow are more likely to collapse over time than those under unidirectional flow. In this study, vessels were only cultured for 5 days, so longer culture times would be needed to confirm this. Studying the process of vasoconstriction might be more difficult in bidirectional flow as SMCs have a contracted morphology before exposure to cytokines.

The addition of SMCs and the application of unidirectional flow yielded a more complex artery-on-a-chip model with a good assay window for fibronectin deposition, lipid accumulation, and ICAM-1 expression that could be used to screen for drug candidates to treat vascular inflammation. Here, inflammation was modeled with the addition of TNFα and IL-1β, which are secreted by activated leukocytes[31] and are proinflammatory triggers linked for atherosclerosis.[65] Additionally, when exposed to inflammatory cytokines, both unidirectional and bidirectional conditions had a significant increase in IL-6 release and ICAM-1 expression, consistent with previous findings.[66–69] This means that both unidirectional and bidirectional conditions provided a significant assay window for evaluating vascular inflammation. In the future, monocytes or other immune cells could be added to both coculture models to mimic the adhesion and extravasation immune component of early-stage atherosclerosis or vascular inflammation.[26]

While this study highlights the effects of flow conditions on monoculture and coculture endothelial vessels, several limitations can be noted. One limitation is that the platform experiences a period of backflow in the unidirectional condition when the fluid is resetting. To date, many of the unidirectional flow microfluidic models are not continuously unidirectional but have a stall or reset phase to allow for the fluid to return to the initial well. While having continuous unidirectional flow would be beneficial, this is not yet feasible in a gravity driven platform, and is a compromise for achieving much higher scalability. It should also be considered some discontinuity in the flow might be acceptable given the pulsatile nature of *in vivo* perfusion due to the heart beating. The OrganoPlate 2-lane-48 UF has a shear of 3.7 dynes per cm^2, which is lower than *in vivo* arteries or some other microfluidic devices used to mimic blood vessels.[35] However, alignment of EC under unidirectional flow was observed.[35–37,39,70,71]

This study presents a novel artery-on-a-chip model that effectively recapitulates key features of healthy and diseased arteries using a medium-throughput microfluidic platform with unidirectional gravity-driven flow. Using the OrganoPlate® 2-lane-48 UF, we demonstrated that unidirectional flow promotes endothelial alignment, reduces fibronectin deposition, and maintains a non-contractile smooth muscle cell phenotype, mimicking a healthy arterial state, while bidirectional flow induces characteristics associated with early endothelial dysfunction, including increased fibronectin secretion, lipid accumulation, and ICAM-1 expression. Exposure to inflammatory cytokines elicited distinct responses under both flow conditions, further highlighting the platform's ability

to model vascular inflammation. The integration of endothelial and smooth muscle cells in this microfluidic environment provides a more physiologically relevant system for studying cardiovascular diseases and evaluating potential therapeutics. Compared to traditional *in vitro* and animal models, this platform offers improved flow control, scalability, and compatibility with lab automation, making it a valuable tool for drug discovery and mechanistic studies. However, some limitations remain, including a brief period of backflow during flow resetting, potential differences in intraluminal shear stress due to vessel contraction, and the relatively short culture duration used in this study. Future research should explore longer culture durations, additional immune components, and further refinements to optimize the model for broader applications in vascular biology and pharmacology.

Data availability

The data supporting this article have been included as part of the ESI.†

Author contributions

HE wrote original draft of the manuscript. TPB, PV and SJT contributed to the methodology of the instrument and software. HE, TO, TPB, and LJvB conceptualized, performed, and analyzed experiments. TPB and LJvB supervised the work and edited the manuscript. All authors contributed to the article and reviewed and approved the submitted version.

Conflicts of interest

HE, TO, SJT, PV, TPB and LJvB are employees of Mimetas B. V., which markets the OrganoPlate and OrganoFlow, and holds the registered trademarks OrganoPlate and OrganoFlow. SJT and PV are shareholder of Mimetas B.V.

Acknowledgements

This project has received funding from the European Union's Horizon 2020 research and innovation program under the Marie Skłodowska-Curie grant agreement No. 813920 LogicLab.

References

1 Cardiovascular diseases (CVDs), **https://www.who.int/news-room/fact-sheets/detail/cardiovascular-diseases-(cvds)**, (accessed 27 October 2022).
2 P. G. Schrag, Global Action: for the prevention and control of noncommunicable diseases, 2019, pp. 1–232.
3 S. Mundi, M. Massaro, E. Scoditti, M. A. Carluccio, V. W. M. Van Hinsbergh, M. L. Iruela-Arispe and R. De Caterina, Endothelial permeability, LDL deposition, and cardiovascular risk factors-A review, *Cardiovasc. Res.*, 2018, **114**, 35–52.
4 R. P. Priyadharsini, Animal models to evaluate anti-atherosclerotic drugs, *Fundam. Clin. Pharmacol.*, 2015, **29**, 329–340.
5 A. J. Lusis, Atherosclerosis, *Nature*, 2000, **407**, 233–241.
6 D. Tousoulis, A. Kampoli, C. Tentolouris, N. Papageorgiou and C. Stefanadis, The Role of Nitric Oxide on Endothelial Function, *Curr. Vasc. Pharmacol.*, 2012, **10**, 4–18.
7 P. J. Little, C. D. Askew, S. Xu and D. Kamato, Endothelial Dysfunction and Cardiovascular Disease: History and Analysis of the Clinical Utility of the Relationship, *Biomedicines*, 2021, **9**, 699.
8 Y. Zhao, P. M. Vanhoutte and S. W. S. Leung, Vascular nitric oxide: Beyond eNOS, *J. Pharmacol. Sci.*, 2015, **129**, 83–94.
9 T. Asakura and T. Karino, Flow patterns and spatial distribution of atherosclerotic lesions in human coronary arteries, *Circ. Res.*, 1990, **66**, 1045–1066.
10 J. J. Chiu and S. Chien, Effects of disturbed flow on vascular endothelium: Pathophysiological basis and clinical perspectives, *Physiol. Rev.*, 2011, **91**, 327–387.
11 C. Wang, B. M. Baker, C. S. Chen and M. A. Schwartz, Endothelial cell sensing of flow direction, *Arterioscler., Thromb., Vasc. Biol.*, 2013, **33**, 2130–2136.
12 S. Chien, Effects of disturbed flow on endothelial cells, *Ann. Biomed. Eng.*, 2008, **36**, 554–562.
13 A. Thomas, H. Daniel Ou-Yang, L. Lowe-Krentz, V. R. Muzykantov and Y. Liu, Biomimetic channel modeling local vascular dynamics of pro-inflammatory endothelial changes, *Biomicrofluidics*, 2016, **10**(1), DOI: **10.1063/1.4936672**.
14 G. L. Basatemur, H. F. Jørgensen, M. C. H. Clarke, M. R. Bennett and Z. Mallat, Vascular smooth muscle cells in atherosclerosis, *Nat. Rev. Cardiol.*, 2019, **16**, 727–744.
15 M. Radenković, M. Stojanović, T. Potpara and M. Prostran, Therapeutic approach in the improvement of endothelial dysfunction: The current state of the art, *BioMed Res. Int.*, 2013, **2013**, 252158.
16 D. N. Atochin and P. L. Huang, Endothelial nitric oxide synthase transgenic models of endothelial dysfunction, *Pfluegers Arch.*, 2010, **460**, 965–974.
17 D. E. Ingber, Human organs-on-chips for disease modelling, drug development and personalized medicine, *Nat. Rev. Genet.*, 2022, **23**, 467–491.
18 M. R. Fielden and K. L. Kolaja, The role of early in vivo toxicity testing in drug discovery toxicology, *Expert Opin. Drug Saf.*, 2008, **7**, 107–110.
19 G. A. Figtree, K. Broadfoot, B. Casadei, R. Califf, F. Crea, G. R. Drummond, J. E. Freedman, T. J. Guzik, D. Harrison, D. J. Hausenloy, J. A. Hill, J. L. Januzzi, B. A. Kingwell, C. S. P. Lam, C. A. MacRae, F. Misselwitz, T. Miura, R. H. Ritchie, M. Tomaszewski, J. C. Wu, J. Xiao and F. Zannad, A Call to Action for New Global Approaches to Cardiovascular Disease Drug Solutions, *Circulation*, 2021, **144**, 159–169.
20 R. Rodriguez-Monguio, E. Seoane-Vazquez and J. H. Powers, A Comparative Assessment of Approvals and Discontinuations of Systemic Antibiotics and Other Therapeutic Areas, *Healthcare*, 2023, **11**, 1759.
21 W. SUN, Y. Q. CHEN, G. A. LUO, M. ZHANG, H. Y. ZHANG, Y. R. WANG and P. HU, Organs-on-chips and Its Applications, *Chin. J. Anal. Chem.*, 2016, **44**, 533–541.
22 S. N. Bhatia and D. E. Ingber, Microfluidic organs-on-chips, *Nat. Biotechnol.*, 2014, **32**, 760–772.

23 S. Kim, W. Kim, S. Lim and J. S. Jeon, Vasculature-on-a-chip for in vitro disease models, *Bioengineering*, 2017, **4**(1), DOI: 10.3390/bioengineering4010008.
24 V. [R-F.-16] Rep. Buchanan, Text - H.R.2565 - 117th Congress (2021-2022): FDA Modernization Act of 2021.
25 118th Congress, Text - H.R.7248 - 118th Congress (2023-2024): FDA Modernization Act 3.0., 2024.
26 X. Zhang, M. Bishawi, G. Zhang, V. Prasad, E. Salmon, J. J. Breithaupt, Q. Zhang and G. A. Truskey, Modeling early stage atherosclerosis in a primary human vascular microphysiological system, *Nat. Commun.*, 2020, **11**, 1–17.
27 K. Hattori, Y. Munehira, H. Kobayashi, T. Satoh, S. Sugiura and T. Kanamori, Microfluidic perfusion culture chip providing different strengths of shear stress for analysis of vascular endothelial function, *J. Biosci. Bioeng.*, 2014, **118**, 327–332.
28 S. L. Beth Roman, L. A. Davidson, U. M. Sonmez, Y.-W. Cheng, S. C. Watkins and B. L. Roman, Endothelial cell polarization and orientation to flow in a novel microfluidic multimodal shear stress generator, *Lab Chip*, 2020, **20**, 4373–4390.
29 F. Garcia-Polite, J. Martorell, P. Del Rey-Puech, P. Melgar-Lesmes, C. C. O'Brien, J. Roquer, A. Ois, A. Principe, E. R. Edelman and M. Balcells, Pulsatility and high shear stress deteriorate barrier phenotype in brain microvascular endothelium, *J. Cereb. Blood Flow Metab.*, 2017, **37**, 2614–2625.
30 D. Shav, R. Gotlieb, U. Zaretsky, D. Elad and S. Einav, Wall shear stress effects on endothelial-endothelial and endothelial-smooth muscle cell interactions in tissue engineered models of the vascular wall, *PLoS One*, 2014, **9**, e88304.
31 A. Yoshimura, Y. Hara, T. Kaneko and I. Kato, Secretion of IL-1 beta, TNF-alpha, IL-8 and IL-1ra by human polymorphonuclear leukocytes in response to lipopolysaccharides from periodontopathic bacteria, *J. Periodontal Res.*, 1997, **32**, 279–286.
32 C. K. Byun, K. Abi-Samra, Y. K. Cho and S. Takayama, Pumps for microfluidic cell culture, *Electrophoresis*, 2014, **35**, 245–257.
33 M. Busek, A. Aizenshtadt, T. Koch, A. Frank, L. Delon, M. A. Martinez, A. Golovin, C. Dumas, J. Stokowiec, S. Gruenzner, E. Melum and S. Krauss, Pump-less, recirculating organ-on-a-chip (rOoC) platform, *Lab Chip*, 2023, **23**, 591–608.
34 D. W. Lee, N. Choi and J. H. Sung, A microfluidic chip with gravity-induced unidirectional flow for perfusion cell culture, *Biotechnol. Prog.*, 2019, **35**, 1–8.
35 Y. I. Wang and M. L. Shuler, UniChip enables long-term recirculating unidirectional perfusion with gravity-driven flow for microphysiological systems, *Lab Chip*, 2018, **18**, 2563–2574.
36 Y. Yang, P. Fathi, G. Holland, D. Pan, N. S. Wang and M. B. Esch, Pumpless microfluidic devices for generating healthy and diseased endothelial, *Lab Chip*, 2019, **19**, 3212.
37 V. Van Duinen, A. Van Den Heuvel, S. J. Trietsch, H. L. Lanz, J. M. Van Gils, A. J. Van Zonneveld, P. Vulto and T. Hankemeier, 96 perfusable blood vessels to study vascular permeability in vitro, *Sci. Rep.*, 2017, **7**, 18071.
38 M. Busek, A. Aizenshtadt, T. Koch, A. Frank, L. Delon, M. A. Martinez, A. Golovin, C. Dumas, J. Stokowiec, S. Gruenzner, E. Melum and S. Krauss, Pump-less, recirculating organ-on-a-chip (rOoC) platform, *Lab Chip*, 2023, **23**, 591.
39 M. Ansarizadeh, H. T. Nguyen, B. Lazovic, J. Kettunen, L. De Silva, R. Sivakumar, P. Junttila, S. L. Rissanen, R. Hicks, P. Singh and L. Eklund, Microfluidic vessel-on-chip platform for investigation of cellular defects in venous malformations and responses to various shear stress and flow conditions, *Lab Chip*, 2025, 10–13.
40 S. J. Trietsch, G. D. Israëls, J. Joore, T. Hankemeier and P. Vulto, Microfluidic titer plate for stratified 3D cell culture, *Lab Chip*, 2013, **13**, 3548–3554.
41 H. Ehlers, A. Nicolas, F. Schavemaker, J. P. M. Heijmans, M. Bulst, S. J. Trietsch and L. J. van den Broek, Vascular inflammation on a chip: A scalable platform for trans-endothelial electrical resistance and immune cell migration, *Front. Immunol.*, 2023, **14**, 1118624.
42 N. R. Wevers, R. Van Vught, K. J. Wilschut, A. Nicolas, C. Chiang, H. L. Lanz, S. J. Trietsch, J. Joore and P. Vulto, High-throughput compound evaluation on 3D networks of neurons and glia in a microfluidic platform, *Sci. Rep.*, 2016, **6**, 1–10.
43 L. de Haan, J. Suijker, R. van Roey, N. Bergers, E. Petrova, K. Queiroz, W. Strijker, T. Olivier, O. Poeschke, S. Garg and L. J. van, A Microfluidic 3D Endothelium-on-a-Chip Model to Study Transendothelial Migration of T Cells in Health and Disease, *Int. J. Mol. Sci.*, 2021, **22**, 8234.
44 Z.-Q. Liu, Scale space approach to directional analysis of images, *Appl. Opt.*, 1991, **30**, 1369.
45 Z. Püspöki, M. Storath, D. Sage and M. Unser, Transforms and operators for directional bioimage analysis: A survey, *Adv. Anat., Embryol. Cell Biol.*, 2016, **219**, 69–93.
46 L. Alzubaidi, J. Zhang, A. J. Humaidi, A. Al-Dujaili, Y. Duan, O. Al-Shamma, J. Santamaría, M. A. Fadhel, M. Al-Amidie and L. Farhan, Review of deep learning: concepts, CNN architectures, challenges, applications, future directions, *Journal of Big Data*, 2021, **8**, 53.
47 P. Vulto, S. Podszun, P. Meyer, C. Hermann, A. Manz and G. A. Urban, Phaseguides: A paradigm shift in microfluidic priming and emptying, *Lab Chip*, 2011, **11**, 1596–1602.
48 V. M. Aguilar, A. Paul, D. Lazarko and I. Levitan, Paradigms of endothelial stiffening in cardiovascular disease and vascular aging, *Front. Physiol.*, 2023, **13**, 1081119.
49 P. F. Davies, K. A. Barbee, M. V. Volin, A. Robotewskyj, J. Chen, L. Joseph, M. L. Griem, M. N. Wernick, E. Jacobs, D. C. Polacek, N. DePaola and A. I. Barakat, Spatial relationships in early signaling events of flow-mediated endothelial mechanotransduction, *Annu. Rev. Physiol.*, 1997, **59**, 527–549.
50 C. K. Choi and B. P. Helmke, Short-Term Shear Stress Induces Rapid Actin Dynamics in Living Endothelial Cells, *Mol. Cell. Biomech*, 2008, **5**, 247.
51 M. J. Levesque and R. M. Nerem, The Elongation and Orientation of Cultured Endothelial Cells in Response to Shear Stress, *J. Biomech. Eng.*, 1985, **107**, 341–347.

52 A. W. Orr, J. M. Sanders, M. Bevard, E. Coleman, I. J. Sarembock and M. A. Schwartz, The subendothelial extracellular matrix modulates NF-κB activation by flow: A potential role in atherosclerosis, *J. Cell Biol.*, 2005, **169**, 191–202.

53 K. J. Moore and E. A. Fisher, The double-edged sword of fibronectin in atherosclerosis, *EMBO Mol. Med.*, 2012, **4**, 561–563.

54 R. E. Feaver, B. D. Gelfand, C. Wang, M. A. Schwartz and B. R. Blackman, Atheroprone Hemodynamics Regulate Fibronectin Deposition to Create Positive Feedback that Sustains Endothelial Inflammation, *Circ. Res.*, 2010, **106**, 1703.

55 K. Fox, J. S. Borer, A. J. Camm, N. Danchin, R. Ferrari, J. L. Lopez Sendon, P. G. Steg, J. C. Tardif, L. Tavazzi and M. Tendera, Resting Heart Rate in Cardiovascular Disease, *J. Am. Coll. Cardiol.*, 2007, **50**, 823–830.

56 C. Poussin, B. Kramer, H. L. Lanz, A. van den Heuvel, A. Laurent, T. Olivier, M. Vermeer, D. Peric, K. Baumer, R. Dulize, E. Guedj, N. V. Ivanov, M. C. Peitsch, J. Hoeng and J. Joore, 3D human microvessel-on-a-chip model for studying monocyte-to-endothelium adhesion under flow – application in systems toxicology, *ALTEX - Alternatives to animal experimentation*, 2020, **37**, 47–63.

57 F. Chapman, L. de Haan, L. Gijzen, W. Strijker, E. T. Sticken, S. J. Pour, R. Wieczorek, F. Haberstroh, S. Otte, T. Nahde, L. Simms and M. Stevenson, Optimisation of an in vitro human cardiovascular model on-a-chip for toxicological assessment of nicotine delivery products, *Front. Toxicol.*, 2024, **6**, 1–16.

58 E. Roux, P. Bougaran, P. Dufourcq and T. Couffinhal, Fluid Shear Stress Sensing by the Endothelial Layer, *Front. Physiol.*, 2020, **11**, 861.

59 M. Morigi, C. Zoja, M. Figliuzzi, M. Foppolo, G. Micheletti, M. Bontempelli, M. Saronni, G. Remuzzi and A. Remuzzi, Fluid shear stress modulates surface expression of adhesion molecules by endothelial cells, *Blood*, 1995, **85**, 1696–1703.

60 A. K. Hiroko Tsuboi, J. Ando, R. Korenaga and Y. Takada, Flow stimulates ICAM-1 expression time and shear stress dependently in cultured HUVEC.pdf, *Biochem. Biophys. Res. Commun.*, 1995, **206**, 988–996.

61 C. Hahn and M. A. Schwartz, Mechanotransduction in vascular physiology and atherogenesis, *Nat. Rev. Mol. Cell Biol.*, 2009, **10**, 53–62.

62 N. Méndez-barbero, C. Gutiérrez-muñoz and L. M. Blanco-Colio, Cellular Crosstalk between Endothelial and Smooth Muscle Cells in Vascular Wall Remodeling, *Int. J. Mol. Sci.*, 2021, **22**, 7284.

63 J. J. Chiu, L. J. Chen, S. F. Chang, P. L. Lee, C. I. Lee, M. C. Tsai, D. Y. Lee, H. P. Hsieh, S. Usami and S. Chien, Shear stress inhibits smooth muscle cell-induced inflammatory gene expression in endothelial cells: Role of NF-κB, *Arterioscler., Thromb., Vasc. Biol.*, 2005, **25**, 963–969.

64 Y. Nakashima, E. W. Raines, A. S. Plump, J. L. Breslow and R. Ross, Upregulation of VCAM-1 and ICAM-1 at Atherosclerosis-Prone Sites on the Endothelium in the ApoE-Deficient Mouse, *Arterioscler., Thromb., Vasc. Biol.*, 1998, **18**, 842–851.

65 L. A. Campbell and M. E. Rosenfeld, Infection and Atherosclerosis Development, *Arch. Med. Res.*, 2015, **46**, 339–350.

66 T. Couffinhal, C. Duplaa, L. Labat, J.-M. D. Lamaziere, C. Moreau, O. Printseva and J. Bonnet, Tumor Necrosis Factor-a Stimulates ICAM-1 Expression in Human Vascular Smooth Muscle Cells, *Arterioscler. Thromb.*, 1993, **13**, 407–414.

67 B. E. Rolfe, J. D. Muddiman, N. J. Smith, G. R. Campbell and J. H. Campbell, ICAM-1 expression by vascular smooth muscle cells is phenotype-dependent, *Atherosclerosis*, 2000, **149**, 99–110.

68 L. Yang, R. M. Froio, T. E. Sciuto, A. M. Dvorak, R. Alon and F. W. Luscinskas, ICAM-1 regulates neutrophil adhesion and transcellular migration of TNF-α-activated vascular endothelium under flow, *Blood*, 2005, **106**, 584.

69 S. J. O'Carroll, D. T. Kho, R. Wiltshire, V. Nelson, O. Rotimi, R. Johnson, C. E. Angel and E. S. Graham, Pro-inflammatory TNFaα and IL-1β differentially regulate the inflammatory phenotype of brain microvascular endothelial cells, *J. Neuroinflammation*, 2015, **12**, 1–18.

70 J. Shao, L. Wu, J. Wu, Y. Zheng, H. Zhao, Q. Jin and J. Zhao, Integrated microfluidic chip for endothelial cells culture and analysis exposed to a pulsatile and oscillatory shear stress, *Lab Chip*, 2009, **9**, 3118–3125.

71 B. Kramer, C. Corallo, A. van den Heuvel, J. Crawford, T. Olivier, E. Elstak, N. Giordano, P. Vulto, H. L. Lanz, R. A. J. Janssen and M. A. Tessari, High-throughput 3D microvessel-on-a-chip model to study defective angiogenesis in systemic sclerosis, *Sci. Rep.*, 2022, **12**, 16930.